Available online at www.sciencedirect.com
SCIENCE DIRECT®

Journal of volcanology and geothermal research

Journal of Volcanology and Geothermal Research 2704 (2003) 1–15

www.elsevier.com/locate/jvolgeores

Scattering from a fault interface in the Coso geothermal field

Jonathan M. Lees *

University of North Carolina, Chapel Hill, Department of Geological Sciences, Chapel Hill, NC 27599-3315, USA

Received 28 January 2003; accepted 24 July 2003

Abstract

Large amplitude, secondary arrivals are modeled as scattering anomalies near the Coso, California, geothermal field. Polarization and ray tracing methods determine the orientation and location of the scattering body. Two models are proposed for the scatterer: (1) a point scatterer located anywhere in a one-dimensional (1-D), layered velocity model, (2) a dipping interface between two homogeneous half spaces. Each model is derived by non-linear, grid search inversion for the optimal solution which best predicts observed travel times. In each case the models predict a nearly vertical scatterer southwest of stations S4 and Y4, each southeast of Sugarloaf Mountain, a large rhyolite dome. The interface model includes five unknown parameters describing the location and orientation of the interface in addition to the S-wave velocity of the half space. The S-wave velocity, 3.25 km/s, agrees with independently derived 1-D models in this area. The large amplitude, vertical impedance contrast interface coincides with steep gradients of heat flow measured near the surface and with structural boundaries observed in surface geology. The reflector is most probably the sharp boundary between the northern part of the field where there is significant fluid flow and the southern part where hydrothermal fluids are absent. The interface coincides with geological boundaries and faults recently observed in this region, most likely representing the hydrothermal barrier which channels hot fluids northward.

Keywords: Coso; California; geothermal; faults; earthquakes; seismic scattering; seismic reflections; wave propagation; geological structure

1. Introduction

The Coso, CA, geothermal area (Fig. 1) is one of a series of geothermal resources along the eastern front of the Sierra-Nevada Range (Duffield and Bacon, 1981; Duffield et al., 1980). The geological setting is tectonically complicated, as this region is in the transition zone between the right-slip San Andreas Fault and the extensional Basin and Range Province (Roquemore, 1980). Numerous rhyolite domes punctuate the landscape and dominate the topography of the Coso field (Fig. 1). Surface geology consists of Mesozoic basement rocks, late Cenozoic volcanic and Quaternary alluvial deposits (Duffield et al., 1980). The Quaternary rhyolitic domes were emplaced on Mesozoic bed rock in the last 1.02 million years and some very young volcanic rocks (0.044–0.055 Myr) are associated with the highest observed heat flows and temperature gradients in the area (Combs,

* Tel.: +1-919-962-0695.
E-mail address: jonathan_lees@unc.edu (J.M. Lees).

0377-0273/03/$ – see front matter © 2003 Published by Elsevier B.V.
doi:10.1016/S0377-0273(03)00281-6

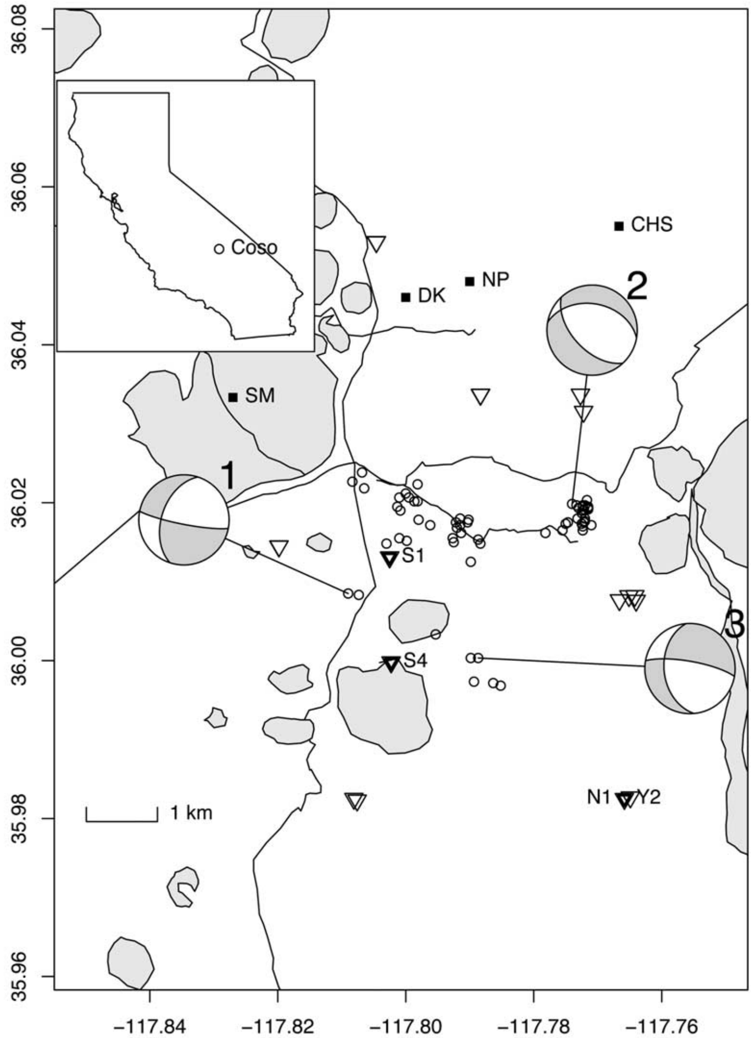

Fig. 1. Areal view of Coso geothermal field with locations of 56 events where phases T_1 and T_2 were observed at station S4. Symbols at events are used to distinguish geographic clusters. Borehole seismic stations are represented by filled triangles. Shaded, circular regions are rhyolite domes provided for geographic orientation. Lines are roads in the geothermal field. The road northeast of station S1 is where P-wave and S-wave seismic lines were shot in 1989. Three focal mechanisms are presented as examples and correspond to seismograms presented in Fig. 3. Geographic registration points include: CHS, Coso Hot Springs; NP, Nicol Prospect; DK, Devil's Kitchen; SLM, Sugarloaf Mountain.

1980). The regional stress field is northeast–southwest compression and southwest–northeast extension, which is reflected in the regional seismicity (Roquemore, 1980).

Extensive geological and geophysical investigations at Coso have been directed towards an accurate evaluation of the geothermal potential (Roquemore, 1980; Walter and Weaver, 1980). The geographic extent of the geothermal reservoir and the heat transport conduits from deep magmatic structures represent important parameters for the economic evaluation of the field. A review of extensive seismic tomography imaging (velocity, attenuation, and anisotropy) of the Coso geothermal field can be found in Lees (2002). The earlier studies were concerned primarily with transmission properties of seismic waves. In this paper we concentrate on reflected waves.

Since 1990 a high resolution, down-hole array has been recording micro-seismicity in the geothermal region. The down-hole array is ideal for recording events of very small magnitude with a high signal–noise ratio since near surface generated signals are diminished relative to incident body waves generated at the source and scattered along the ray path. This provides a valuable tool for investigating, at high spatial resolution, structures associated with the geothermal field, namely delineation of the fault system and structural features associated with hydrothermal flow. Injection within the perimeter of geothermal wells induces multiplet seismicity which illuminates individual cracks along which fluids migrate and transport heat to the surface (Lees, 1998). The intense low magnitude seismicity has been reviewed by Feng and Lees (1998) where stress distribution in the field was partitioned into blocks differing by varying levels of horizontal stress with the smallest vertical principle component of stress occurring in the southwest between stations S4 and S1. Inversion for velocity and attenuation suggests that a low attenuation, low velocity body extends from 4–5 km depth southwest of the field towards the surface where it shoals near Coso Hot Springs and Devil's Kitchen (Fig. 1) to the north (Wu and Lees, 1996; Wu and Lees, 1999). Fluid flow, as estimated by geochemical isotope analysis, indicates rapid hydrothermal transport from deep within the section south of the field towards the north (Leslie, 1991). On the other hand, heat flow is highest near station S1 by Sugarloaf Mountain (Fig. 1), and exhibits a steep gradient south and southwest of station S4 (Combs, 1980). These factors suggest significant structural variations in the field associated with intense fluid and heat transport from deep levels in the south extending to shallow and surface expressions to the north and northeast (Lees, 2002). In this paper scattering off faults or fluid accumulations that have large impedance contrasts relative to local country rock are shown to produce secondary arrivals in P- and S-wave codes.

In 1989 two vertical motion and one shear motion vibroseismic reflection lines were shot through the geothermal field (Malin and Erskine, 1990). The P-wave lines showed clear, nearly horizontal reflectors at 2.3–2.5 s (two-way travel time) and the S-wave lines had reflections, away from the field, at 4.1–4.3 s (Caruso and Malin, 1993). These reflectors are mapped to depths of 5–6 km, which correspond to the bottom of the seismically active zone in the geothermal field. (Deeper, less coherent reflections were also observed on the P-wave lines.) Some researchers argue that reduction of seismicity at this depth is a result of transition to the more ductile, high temperature regime near the primary heat source and magma supply (Lees, 2002). By contrast, secondary reflections presented in this paper typically occur 0.5242–1.1924 s after earthquake origin for the P-waves and 1.0807–2.1193 s for S-waves, considerably sooner than expected for reflections off deeper interfaces. In the discussion that follows, it is shown that reflections observed at the southerly micro-earthquake stations (particularly station S4), emanate from steeply dipping interfaces south of the producing geothermal field.

2. Data selection and reduction

The data used in this paper come from several clusters recorded on a high frequency down-hole network installed by the Navy Geothermal Office and CalEnergy Co. (Fig. 1). The down-hole seismometers are typically buried at 70–90 m depending on temperature and drilling conditions. The acquisition sample rate is 480 samples/s and the signal-to-ratio is generally high due to noise reduction by being removed from the surface. In the 1993–1995 period, over 2500 high quality events were recorded on more than eight stations of the down-hole array. (High quality events are located with small estimated error, low root-mean-square (RMS) misfit, and small station gap.) Typical events range in magnitude from −1 to 3, with a majority of events used in this study in the 0–1 range. Events were located with a one-dimensional (1-D) model (Table 1) with horizontal errors of 70 m and depth errors of 100 m. Those that formed clusters were relocated with high precision using cross correlation methods (Lees, 1998).

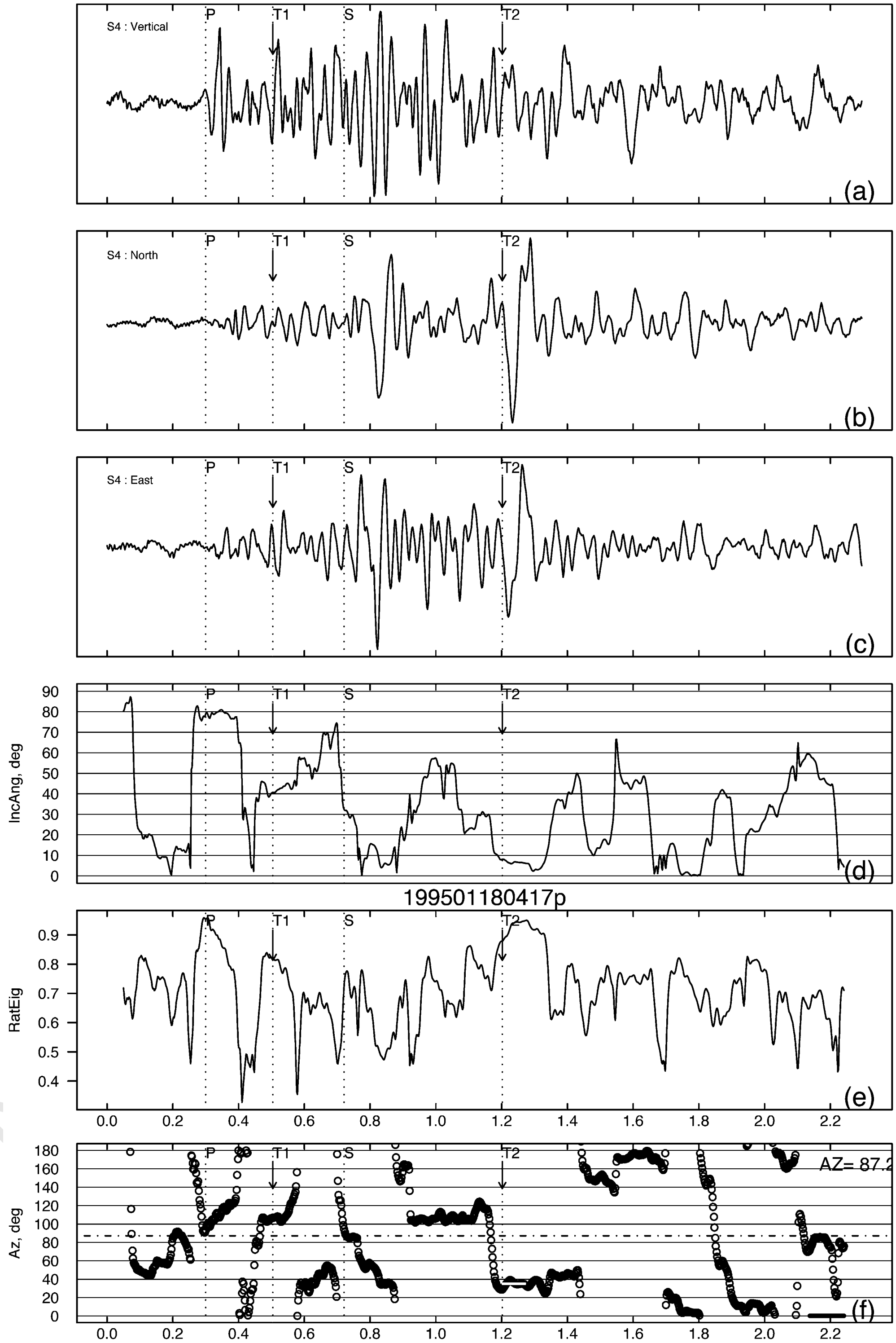
S4 : Vertical
P
T1
S
T2
(a)
S4 : North
(b)
S4 : East
(c)
IncAng, deg
(d)
199501180417p
RatEig
(e)
Az, deg
AZ= 87.2
(f)

Table 1
Coso regional velocity model

Z (km)	P (km/s)	S (km/s)
0	4.5	2.43
0.5	4.51	2.59
1	4.92	2.97
2	5.46	3.15
3	5.54	3.27
4	5.58	3.42
12	6.05	3.49
20	7.2	4.15
30	8	4.62

These form the underlying database from which events chosen for this study are drawn. Events fall into several spatial clusters associated with fluid flow and stress distribution in the geothermal field (Feng and Lees, 1998). Some of the seismicity, particularly that found near focal mechanism 2 in Fig. 1, is closely correlated to injection in the geothermal field. Among the 2500 events in the high quality database, numerous events exhibited unusually high amplitude arrivals (T_1) in the P-wave code (prior to the S-wave arrival) in addition to an arrival (T_2) approximately 0.4–0.5 s after the S-wave arrival. (Designation of the phase arrival names T_1 and T_2 is arbitrary.) While several hundred events were examined, not all the events exhibited these unusually large secondary arrivals, nor were these seen on all the stations. In this paper, signals recorded at station S4 are mainly used, where secondary arrivals were most clearly observed, although stations Y2/N1 showed similar secondary arrivals. Among the hundreds of events inspected, 145 events had recordings of either T_1 or T_2. At station S4, 92 events had T_1 arrivals in the P-wave code and 35 events showed clear T_2 arrivals. The travel time differentials of these data are used to model the geometry of the scattering interface.

A sample three-component seismogram recorded at station S4 is presented in Fig. 2a–c. The time series were selected from a 2 s window starting 0.1 s from the onset of the P-wave. (P-wave and S-wave arrivals are represented by vertical, dashed lines, T_1 and T_2 arrivals are indicated by arrows.) There is a clear P-wave arrival recorded on the vertical component with S arrivals prominent on the horizontal components. A prominent signal indicated by T_1 arrives 0.2 s after the direct P-wave and a secondary signal, T_2, is recorded about 0.4 s after the direct S-wave. Note the large relative amplitudes of the secondary T_1 and T_2 signals compared to direct P and S, respectively. To estimate local particle motion, a moving, 50 sample (0.1 s) window was used to determine direction and linearity of motion for each arrival (Fig. 2d–f). Within each window principal directions were estimated by eigenvalue decomposition of the vector field particle motion. Averages of the incident angle and azimuth were then determined following each of the four arrivals studied here. Ratios of eigenvalues were used to quantify the level of linear motion for each arrival. In nearly all the samples the arrival of phase T_2 was highly linear, as compared to the more erratic arrivals of the corresponding S-wave. No correlation was found between any of the particle motion azimuths determined in this way, nor was there any appreciable correlation with back azimuth to the corresponding event.

Rotated seismograms are provided in Fig. 3 for three example events. Particle motion plots (hodograms) are provided for each case and focal mechanisms for these events are displayed in Fig. 1. The bottom panel is the same event as that provided in Fig. 2, showing radial and transverse components and particle motion. As mentioned above, no consistent pattern was observed relating particle motion of T_1 to P or T_2 to S. To

Fig. 2. Sample three-component seismogram recorded at station S4. Phase arrivals for P and S are marked by vertical lines. T_1 and T_2 are labeled on the vertical and north components, respectively. Note the amplitude of T_1 is larger than the direct arrival, P. (a) Vertical component. (b) North component. (c) East component. Lower panels represent summaries of particle motion along the trace. (d) Estimated angle of incidence at the station. (e) Estimate of the quality of linearity of particle motion. (f) Estimated azimuth measured from north. After arrival of phase T_2 the azimuth is stable at about 35°. The focal mechanism for this event is number 3 in Fig. 1.

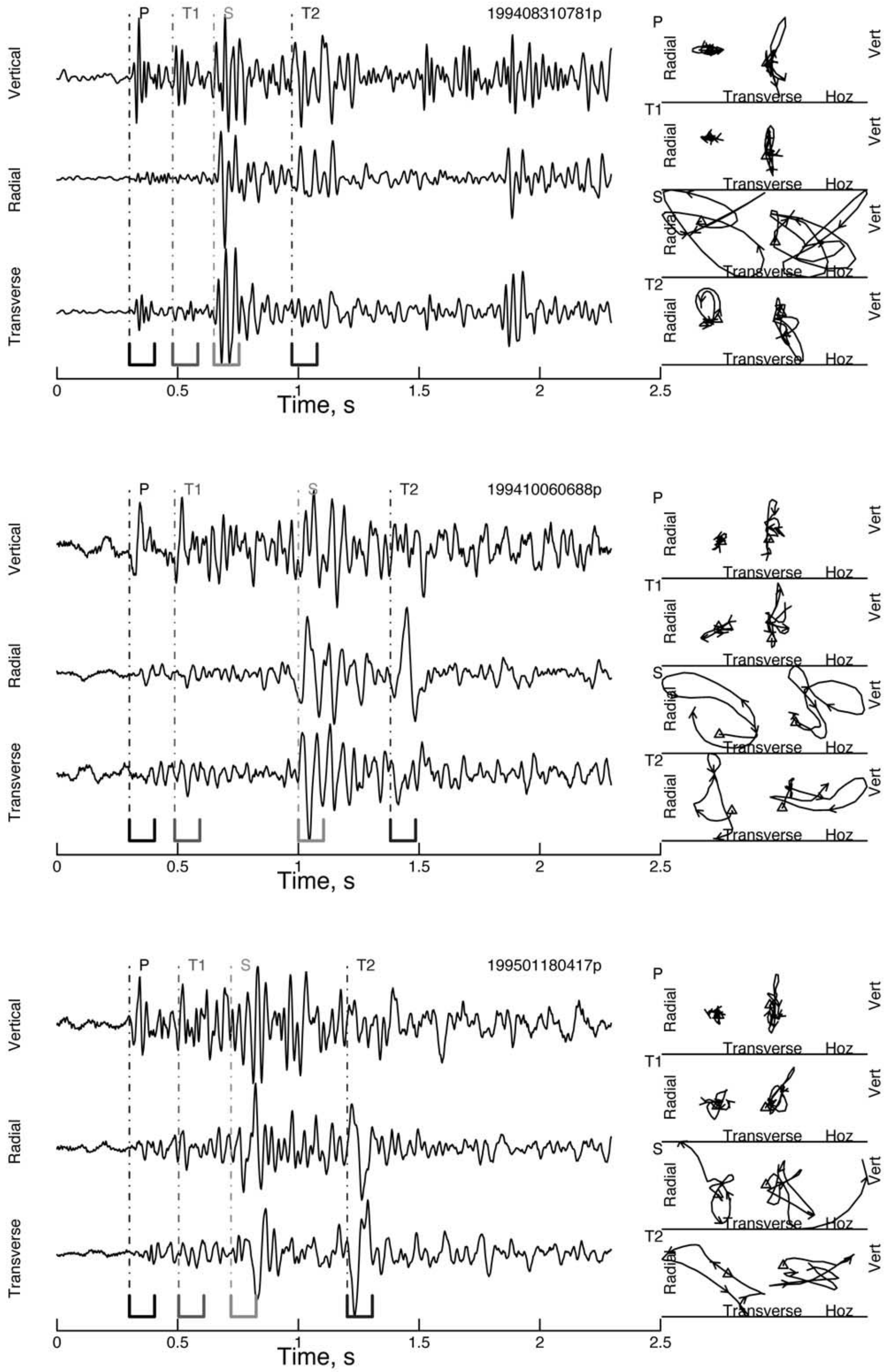

P
T1
S
T2
199408310781p
199410060688p
199501180417p
Vertical
Radial
Transverse
Time, s
0
0.5
1
1.5
2
2.5
Vert
Hoz

assess the influence of radiation pattern on the relative amplitudes of these arrivals, observed amplitude ratios were plotted against predicted amplitude ratios from focal mechanisms. Predicted ratios for either P-, SH- or SV-waves showed virtually no sensitivity to observed amplitude ratio of T_2 to S, or T_1 to P.

3. Scattering location

Two independent approaches are proposed for determining parameters describing a potential reflector model based on a grid search through model space. The approach taken here is similar to analyses used in other volcanic regions (Ammon et al., 1989; Matsumoto and Hasegawa, 1996; Stroujkova and Malin, 2000). In each case a small set of parameters is derived, parameterizing a reflecting boundary through grid search of models that predict the travel times. The grid search evaluates the ability of each model to predict the RMS travel time from source to station after scattering at the reflecting body. The preferred model is that which minimizes the RMS travel time for all the data exhibiting secondary (T_1 and T_2) arrivals.

Consider first a model consisting of a layered half space following the 1-D model used for event locations. A single point scatterer is assumed to exist somewhere in the vicinity of the station and P- and S-waves propagating through the media interact once with the scatterer (Fig. 4a). This simplified model assumes that all signals diffract at the same location in the earth. A grid search is used to locate the position of that scattering point which best predicts the observed travel times of the data (T_1 or T_2). This technique is similar to, although simpler than, that employed by Stroujkova and Malin (2000) where waveforms were migrated by summing over data windows. Rays are traced in the 1-D model from source to scatterer and then from scatterer to receivers at the surface. Since it is not known a priori whether the scattering includes S-S, S-P, P-S, or P-P the point models for all these combinations were calculated. The S-S model for T_2 seems most appropriate, though, since the scattered waveforms so often appear to mimic the S-wave arrival waveform. The results, showing a cloud of RMS (RMS of observed minus calculated travel times) values is provided in Fig. 5. Dark squares in the figure are determined independently and represent locations in space which predict low RMS misfit of travel time data. A point at the surface located southwest of S4 was the absolute minimum for this model although it appears that numerous other locations were nearly as good, as observed by the smeared region of nearly equal values in Fig. 5. Potential scatterers form a concave hull around station S4 facing to the northeast. The shape of this image resembles the scattering envelope (Sato and Fehler, 1998) of an S-S reflection, although since numerous events are used it can be considered an intersection of all the scattering envelopes for station S4.

The presence of a rhyolite dome at the surface offers one interpretation: the large velocity contrast near the surface between sediments and the rhyolite volcanics could provide a locus for the significant scattering observed. Other rhyolite domes in this region, like the much larger Sugarloaf Mountain (Fig. 1), do not, apparently, produce observable scattering of this magnitude. The frequencies of the signals discussed in this paper are approximately 25–35 Hz for T_1 and 15–20 Hz for T_2. Assuming a typical S-wave velocity of 3 km/s, we expect these signals to be sensitive to bodies that are on the order of 150 m or larger. It is thus unlikely that the simple, single scattering

Fig. 3. Three examples of arrivals at station S4. Focal mechanisms 1–3 in Fig. 1 correspond to the top, center and bottom of this figure. The seismograms have been rotated into vertical, radial, transverse motion according to the back azimuth to the source. Hodograms (particle motion displays) are on the right and correspond to motion in the time windows indicated on each seismogram on the left. Radial transverse motion for each arrival is presented on the left and vertical–horizontal is presented on the right (horizontal motion is the RMS amplitude of the radial transverse motion). The bottom panel (event 3 in Fig. 1) corresponds to the unrotated signals presented in Fig. 2.

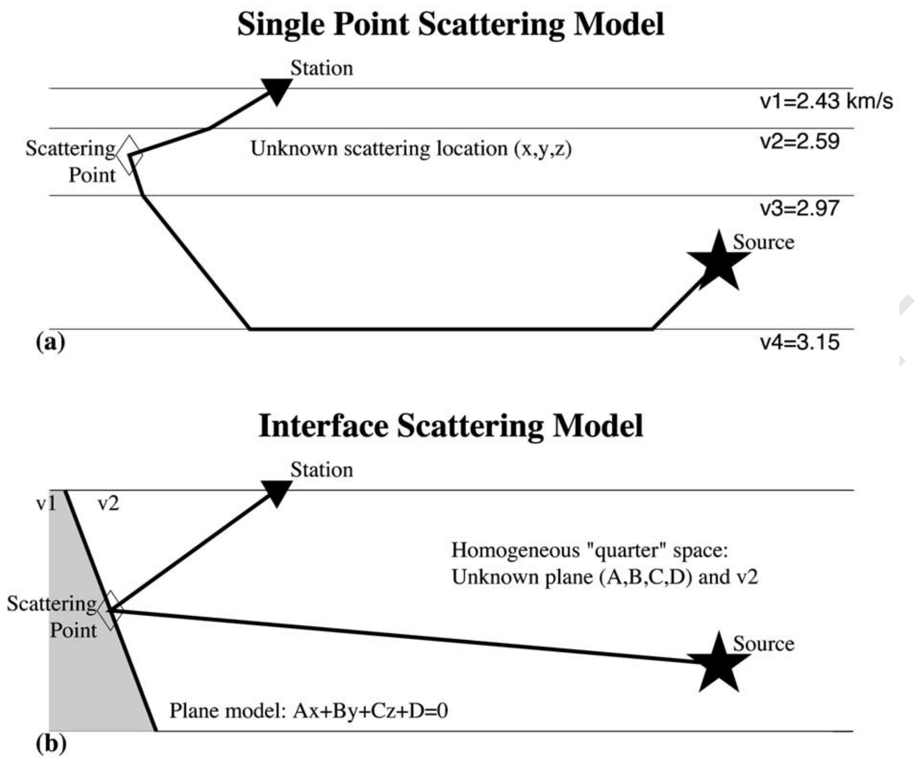

Fig. 4. Synthetic models for estimating travel times. (a) Schematic model showing how the single scattering model is calculated. Travel times from a point source are calculated to a scattering point and then to the station. The RMS residual travel time for each grid point in the model is calculated and used to determine the best fit scattering location. P- and S-wave velocities are provided in Table 1. (b) Schematic model showing how the interface model is represented. A planar fault model is used to determine the best fitting plane that predicts the travel time data. A simple quarter space velocity model is used to predict incident angles and travel times.

model is the actual source of these signals. Furthermore, the possibility of these observed phases being scattered at the surface is ruled out: even though the seismometer is buried at 70 m depth, the T_2–S time difference is too long (0.4 s), requiring an unreasonably low S-wave velocity. A surface reflection would also not explain why these phases are not present at other sites in the network.

An alternative model is a fault plane, dipping at some unknown angle, in an unknown location, as was done by Matsumoto and Hasegawa (1996). In this case, to simplify calculations, the model consists of two quarter spaces that have a large, unknown impedance contrast (Fig. 4b). At this stage the size of the impedance contrast is not the focus, but rather its location and spatial orientation are derived. For completeness the S-wave velocity in the medium is left as an unknown and will be an additional parameter in the inverse modeling. The inverse problem has five unknowns: four associated with the dipping interface, represented by the equation of a plane in space (A, B, C, D):

$$Ax + By + cz + D = 0$$

and one parameter V_S for the S-wave velocity in the medium in which the ray is traveling. Again a grid search is used to find the optimal set of five parameters which best predicts the observed travel times for T_2. The solution was $A = 0.9$, $B = 0.65$, $C = -0.05$, $D = 1.5$, $V = 3.25$ km/s and is shown in Fig. 6, in plan view and cross section respectively.

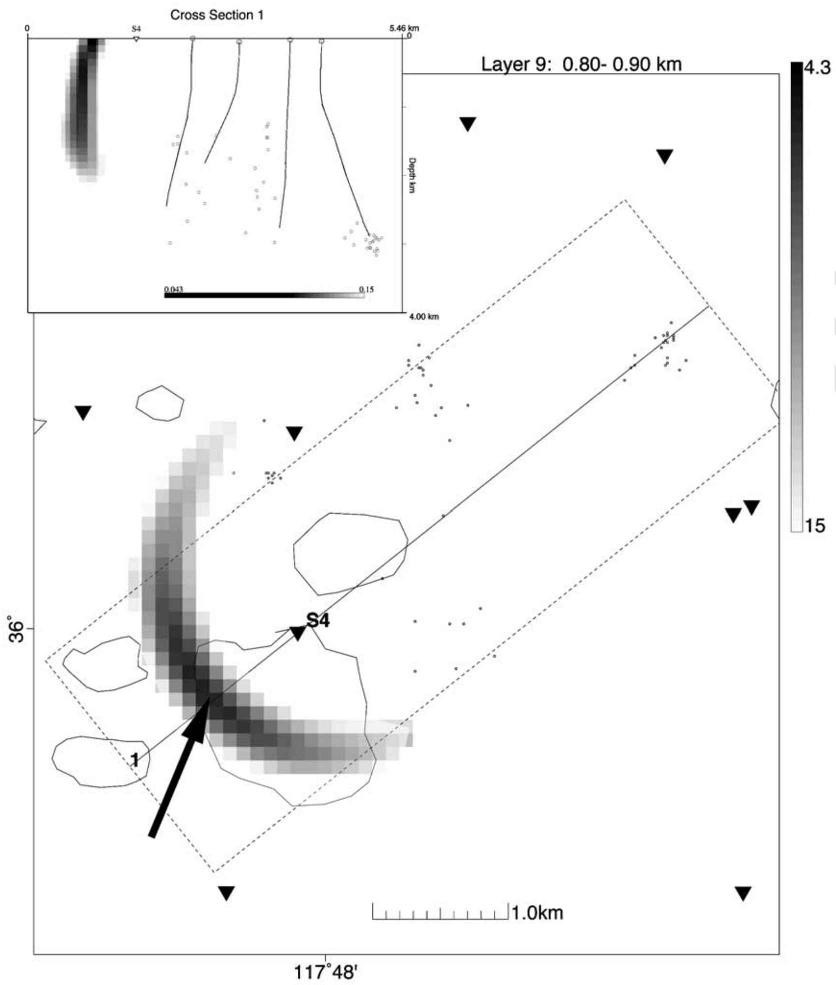

Fig. 5. Horizontal slice at 0.8 km depth through the image of mean square scores provided by the single scatter point model (Fig. 4a). Dark boxes represent low misfit values and likely locations for the scatterer. The smeared out region of relatively low values means that many solutions equally fit the data. Inset is a vertical cross section through the model for the box labeled 1 in the map view. The arrow points to the location with the lowest RMS predicted residual.

The plane appears to be slightly dipping, facing northeast with azimuthal strike trending northwest–southeast. The S-wave velocity estimate of 3.25 km/s is a reasonable average for the field where 1-D velocities range from 2.43 km/s at the surface to 3.42 km/s at 4 km depth. Note that the fault plane is close to, but not coincident with, the possible single scattering points. This may be due to the crude, quarter space velocity model used in the plane calculation as opposed to the finer 1-D layered models used in event location. Also, the RMS of the single scattering model was about half that of the plane model, perhaps due to the same approximation. The most likely scenario for this scattering surface is probably some combination of these two models: a small, localized, planar surface, perhaps not even perfectly flat located about 1 km southwest of S4. One interpretation is that a high impedance fluid/rock contact exists between 1 and 2 km depth in this region, which coincides with a permeability barrier in the southern extent of the producing

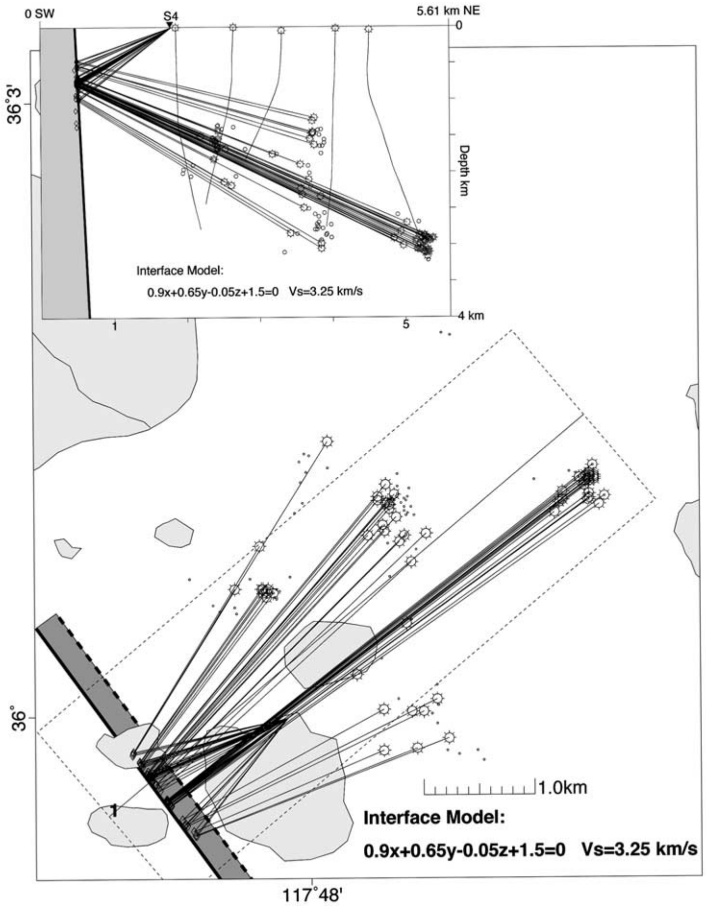

Fig. 6. Plan view of a fault interface model predicted by grid search inversion (Fig. 4b). The interface is projected to the surface with a solid bold line at $z = 0$ (left boundary) and a dashed bold line at $z = 5$ (right boundary). The plane is dipping to the northeast. Lines connecting epicenters to the plane and station represent reflected ray paths projected on the horizontal. Inset is a vertical cross section of the model and bounce points taken along the dashed box labeled 1 in the map view.

field (Frank Monastero, personal communication). Fluids injected north of the field do not penetrate this boundary to the south, producing a concentration of fluids. The large impedance contrast associated with fluid accumulations provides an explanation for the large reflections of positive polarity observed at stations S4 and N1.

Other than station S4, only stations N1 and Y2, southeast of S4, showed similar high amplitude scattering in the S-wave code of any significance. While observations at these stations are not as extensive as those at S4, the T_2 arrivals are unambiguous. Plane interface modeling of these also suggests the presence of a scattering surface southwest of N1, although the planes derived from the Y2 versus the N1 data dip in different directions (Fig. 7a). These inconsistencies are attributed to the small sample of noisier data recorded at these stations relative to station S4. If the varying dip is disregarded, we may assume these are the same scattering surfaces extending southeast from S4 to N1. This orientation is consistent with surface expressions of mapped faults that generally exhibit NNE–SSW strike (Duffield et al., 1980; Roquemore, 1980), and specifically coincides with the mapped Wilson Canyon Fault (Whitmarsh, 1997). If major hydrothermal flow extends from the south to the north in the

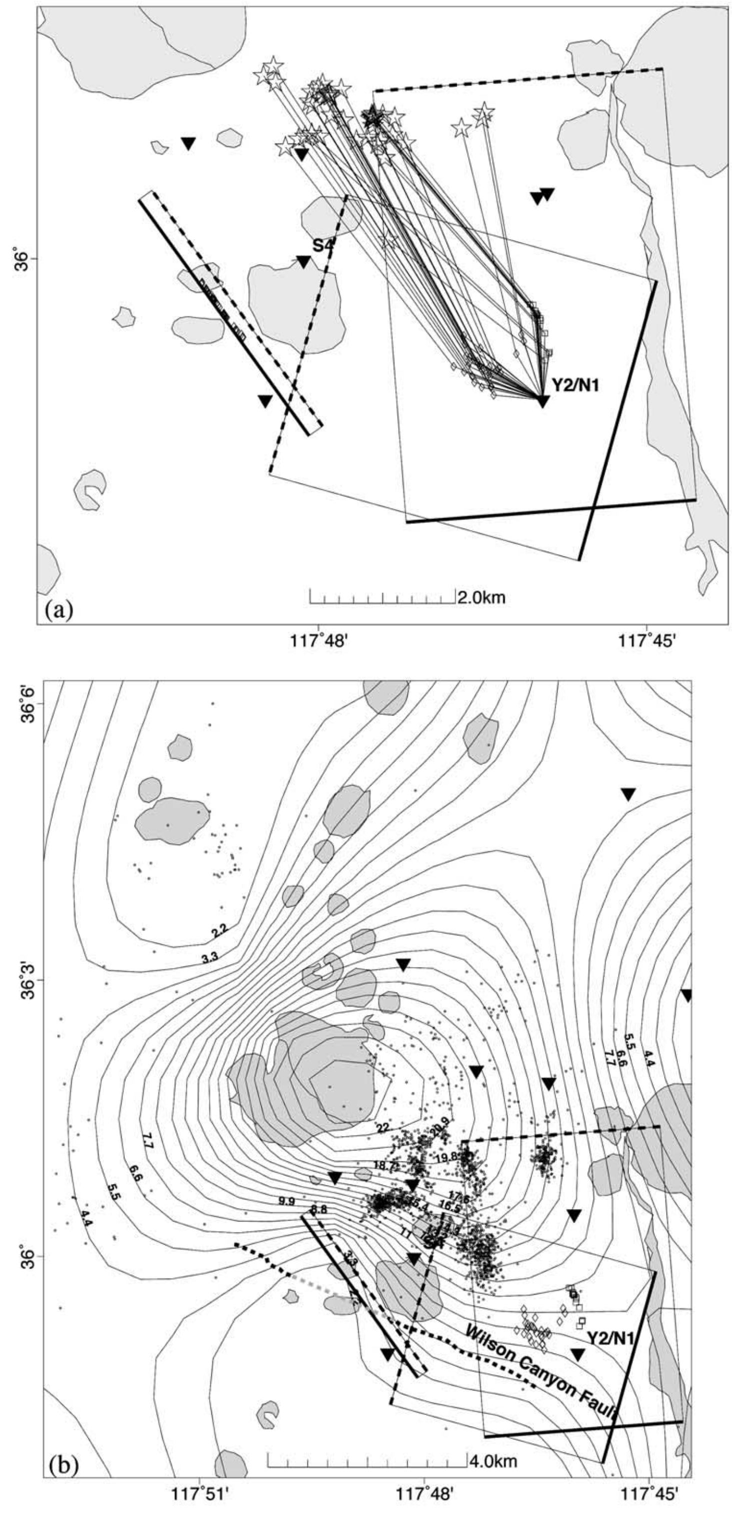
S4
Y2/N1
2.0km
(a)
36°
117°48'
117°45'
36°6'
36°3'
36°
Wilson Canyon Fault
Y2/N1
4.0km
(b)
117°51'
117°48'
117°45'

CGF, as suggested by geochemical analysis (Leslie, 1991), then this analysis may have identified a major, unmapped, buried fault which acts as a primary transport conduit. It is interesting to compare the imaged planes with contours of heat flow in the region (Combs, 1980). Fig. 7b shows the planes superimposed on heat flow contours between 15 and 65 m depth. Notice that the flow contours parallel the S4 plane quite well. Actually the S4 fault plane follows the flow pattern more closely than mapped faults in this region (Whitmarsh, 1997), suggesting that subsurface expression of the fault may be oriented in a more northerly direction southwest of S4, than the mapped surface faults indicate. The conflicting planes associated with N1 and Y2 are more gently dipping and do not have such a simple explanation. It should be noted that bounce points for the N1–Y2 planes (Fig. 7b) are below the region where heat flow contours turn and flatten out. It may be that the boundary in this area is indeed less steeply dipping, although the surface projections of the planes, as derived, do not exhibit a strong correlation with contours as was seen for S4 reflections.

4. Discussion

If the reflection model discussed above is correct, we can use the travel time data to estimate elastic properties of the quarter space between the reflecting surface and the station. Consider the ratio of seismic P- and S-wave velocities in the quarter space:

$$R = V_P/V_S = \frac{D_P \Delta t_P}{D_S \Delta t_S}$$

where V_P, V_S are the respective P- and S-wave velocities, D_P, D_S are the distances to travel for

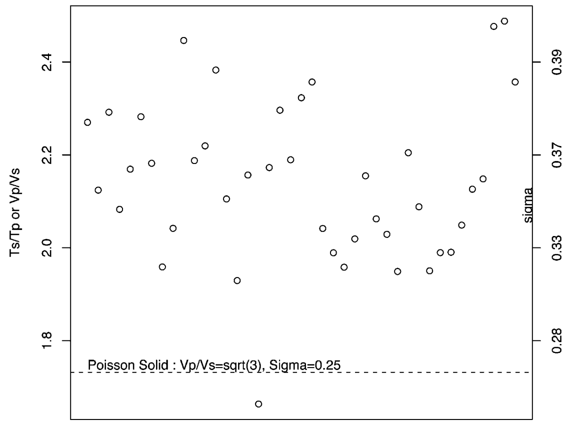

Fig. 8. Plots of V_P/V_S ratio as represented by the time differential between the converted P- and S-waves and the corresponding P and S arrivals. Dashed line represents the commonly assumed Poisson's solid for rocks where $V_P/V_S = \sqrt{3}$, or Poisson's ratio, $\sigma = 0.25$. The right side scale is in units of σ.

each phase and $\Delta t_P = T_1 - T_P$, $\Delta t_S = T_2 - T_S$ are the differences between travel times of the corresponding converted phases and the direct arrivals. Assuming the ray paths are nearly coincident over the small distance considered here, we have $D_P = D_S$, and $R = \Delta t_S / \Delta t_P$, which is presented in Fig. 8. The R ratios vary primarily between 1.93 and 2.45, fairly high compared to most crustal rocks, and considerably higher than previous R estimates at Devil's Kitchen of 1.57 (Combs and Rotstein, 1976; Walck, 1988; Wu and Lees, 1999). Devil's Kitchen is a shallow geothermal feature where fumaroles and hot gases bubble at the surface. The higher R southwest of station S4 is considerably deeper, perhaps 1–2 km depth. Converting the V_P/V_S to Poisson's ratio (Fig. 8) by:

$$\sigma = \frac{R^2 - 2}{2 * (R^2 - 1)}$$

Fig. 7. (a) Plan view of interface planes derived for data recorded at stations Y2 and N1. Ray paths and bounce points are illustrated. Note the planes dip in different directions, but the bounce points are clustered near each other. The solid bold line on each interface shows the intersection of the plane with surface ($z = 0$) and the dashed bold line shows the intersection of the interface with $z = 5$ km depth. The lateral extent of the interface is arbitrary and is shown as a schematic. (b) Plan view of interface planes with heat flow contours measured between 15 and 65 m depth (Combs, 1980). Squares and diamonds represent bounce points for the two derived planes.

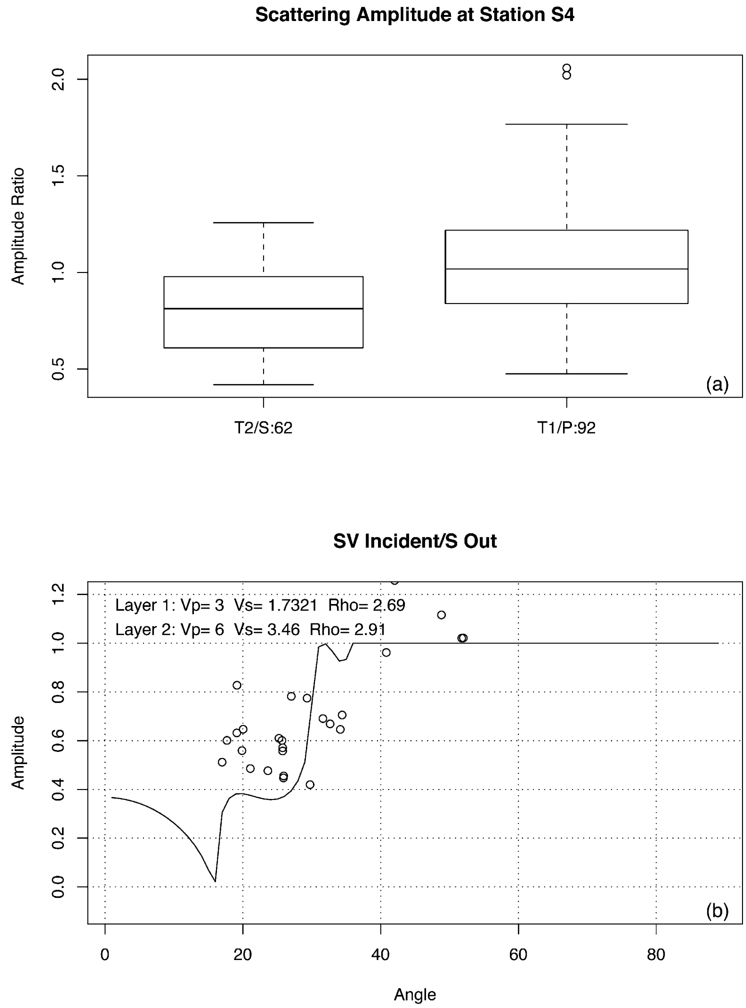

Fig. 9. (a) Box plots of absolute amplitudes of T_2 versus direct S (left) and T_1 versus direct P (right). Absolute amplitudes are estimated by taking the RMS of particle velocity over a short time window encompassing the arrivals. Box plots show the median value (center line in box), the quartiles (box) and octiles (horizontal bars) of the distribution of values. Outliers lie beyond the octiles. The median value of T_1/P amplitudes is greater than the T_2/S amplitude ratios and the data scatter is larger. (b) T_2/S ratio versus incident reflection angle for an incident SV-wave. Note the apparent increase in amplitude ratio with increase in incident angle. Also plotted for reference are theoretical results from Zoeppritz equations. The theoretical model consisted of two layers: the layer with the incident wave consisted of: $V_P = 3$ km/s, $V_S = 1.732$ km/s and density $\rho = 2.69$ kg/m^3. The layer outside the geothermal field had: $V_P = 6$ km/s, $V_S = 3.46$ km/s and $\rho = 2.91$ kg/m^3.

we have σ ranging from 0.32 to 0.40, also elevated compared to the commonly assumed $\sigma = 0.25$ for a Poisson's solid. Since $\sigma = 0.5$ for a fluid, the elevated σ values in the region southwest of station S4 suggest the presence of high levels of fluid saturation.

To assess the relative energy at phase arrivals along seismic records, three-component amplitudes were calculated by considering the maximum of the RMS sum of the three components in a small window encompassing each arrival. Focal mechanisms for most events in this study are not well constrained, so correction for radiation differences between direct and reflected arrivals is difficult. No significant correlation between predicted radiation amplitude ratios for waves emerging towards S4 versus the reflection points and corresponding observed amplitude ratios of either T_2 versus S or T_1 versus P arrivals was found in this data set. This is certainly partly due to the fact that many of the earthquakes have very similar azimuths and take off angles to station S4 and to the reflecting points. The correlation is certainly decreased by the poorly constrained focal mechanism, which makes proper radiation corrections difficult.

Estimates of relative amplitudes of T_1 and T_2 arrivals compared to P- and S-wave amplitudes (see example in Fig. 2) indicate a large impedance contrast (Fig. 9a). Given the large attenuation observed in this part of the field (Wu and Lees, 1996), the extra distance the secondary arrival must travel would normally produce a considerably smaller amplitude than those observed at station S4 for the T_1 and T_2 signals. In some cases, amplitudes of secondary arrivals (T_1, T_2) are greater than the direct arrivals by a factor of 2, suggesting that focusing from a curved surface plays an important role in modeling these signals. This implies that the simple scattering models described above are not adequate. The shape of the single scattering field is concave facing station S4, an artifact of the method that relies on only one station for imaging. It may be possible to combine the two scattering models presented above into a more general focusing interface. Kirchoff–Helmholtz synthetic seismograms (Frazer, 1987), integrated over the focusing surface, could then be used to compare model predicted amplitudes with observations. Synthetic simulations of seismic arrivals, however, are beyond the scope of this paper and will be pursued in subsequent studies. The observed large amplitude ratios still require significant variations in elastic rock properties across the boundary. Phase reversals are not especially evident, suggesting that the proposed interface has a positive reflection coefficient, i.e. waves arrive in lower impedance material and reflect off a higher impedance quarter space. There appears to be a positive correlation of incident angle at the reflection point on the dipping interface south of S4 and T_2/S amplitude ratio (Fig. 9b). This is generally consistent with Zoeppritz relations of energy partition at a reflecting interface with incident SV-waves (Fig. 9b). While the modeling is crude, the apparent correlation of the incident angles to the theoretical prediction based on a simple reflection at the dipping interface is compelling. The exact amplitude relationship is not duplicated since effects of focusing, and other scattered code arrivals, distort amplitudes considerably. While amplitude ratios are derived directly from the digital data, incident angles are determined from the models described above, and so are predicated on assumptions underlying the calculations. For example, the assumption of a homogeneous (or any other derived) velocity field will introduce a bias in the angle calculations. The direct ray in the quarter space model should underestimate the angle since a 1-D velocity model, that increases with depth, will tend to bend rays downward from source to reflection point, increasing the incident angles. In spite of all these caveats, the consistency of the simple theoretical predictions and observations is remarkable, and so provides strong support for the scattering model.

5. Conclusion

Secondary arrivals in the P- and S-wave code of numerous events in the Coso geothermal field suggest subsurface scattering may be important. Travel time residuals for two very different models suggest that a scattering interface exists southwest of station S4, south of Sugarloaf Mountain (Fig. 1). The point scattering model for S-S conversion predicts a cloud of loci where a single scattering point in a 1-D, layered velocity model produces the scattering. A planar scatterer, on the other hand, predicts an interface trending northwest–southeast dipping steeply about 1.0 km southwest of station S4. High V_P/V_S ratios and large impedance contrast across the potential reflector suggest a saturated fluid/rock interface, perhaps associated with hydrothermal circulation.

Acknowledgements

The author thanks the Navy Geothermal Program for funding this project (award #N68936-94-R-0139) and providing data. I further acknowledge CalEnergy Co. Inc. and Peter Malin (Duke University) for data and valuable comments. Two anonymous reviewers provided helpful comments and suggestions.

References

Ammon, C.J., Zucca, J., Kasameyer, P., 1989. An S-to-P converted phase recorded near Long Valley/Mono Craters region, California. J. Geophys. Res. 94, 17721–17727.

Caruso, C.W., Malin, P.E., 1993. Structure of the Coso Geothermal Field, Southern California, from seismic reflection and refraction data. EOS Trans. Am. Geophys. Un. 74, 413.

Combs, J., 1980. Heat flow in the Coso geothermal area, Inyo County, California. J. Geophys. Res. 85 (B5), 2411–2424.

Combs, J., Rotstein, Y., 1976. Microearthquake studies at the Coso Geothermal Area, China Lake, California. In: Proceedings of the 2nd United Nations Symposium on the Development and Use of Geothermal Resources, San Francisco, CA, pp. 909–916.

Duffield, W.A., Bacon, C.R., 1981. Geologic map of the Coso volcanic field and adjacent areas, Inyo County, CA. USGS, p. 1.

Duffield, W.A., Bacon, C.R., Dalrymple, G.B., 1980. Late Cenozoic volcanism, geochronolgy, and structure of the Coso Range, Inyo County, California. J. Geophys. Res. 85 (B5), 2381–2404.

Feng, Q., Lees, J.M., 1998. Microseismicity, stress, and fracture within the Coso geothermal Field, California. Tectonophysics 289, 221–238.

Frazer, L.N., 1987. Synthetic seismograms using multifold path integrals – I. Theory. Geophys. J. R. Astron. Soc. 88, 621–646.

Lees, J.M., 1998. Multiplet analysis at Coso Geothermal. Bull. Seismol. Soc. Am. 88, 1127–1143.

Lees, J.M., 2002. Three-dimensional anatomy of a geothermal field. In: Glazner, A., Walker, J.D., Bartley, J.M. (Eds.), Geologic Evolution of the Central Mojave Desert and Southern Basin and Range. Geological Society of America, Boulder, CO, pp. 259–276.

Leslie, B.W., 1991. Decay series disequilibria applied to the study of rock–water interaction in the Coso Geothermal Field, California. Ph.D. Thesis, University of Southern California, 324 pp.

Malin, P.E., Erskine, M.C., 1990. Coincident P and SH reflections from basement rocks at Coso geothermal field. Am. Assoc. Petrol. Geol. Bull. 74, 711.

Matsumoto, S., Hasegawa, A., 1996. Distinct S wave reflector in the midcrust beneath Nikko-Shirane volcano in the northeastern Japan arc. J. Geophys. Res. 101, 3067–3083.

Roquemore, G., 1980. Structure, tectonics, and stress field of the Coso Range, Inyo County, California. J. Geophys. Res. 85 (B5), 2434–2440.

Sato, H., Fehler, M.C., 1998. Seismic Wave Propagation and Scattering in the Heterogeneous Earth. Springer, New York, 308 pp.

Stroujkova, A.F., Malin, P.E., 2000. A magma mass beneath Casa Diablo? Further evidence from reflected seismic waves. Bull. Seismol. Soc. Am. 90, 500–511.

Walck, M.C., 1988. Three-dimensional variations in shear structure and Vp/Vs for the Coso region, California. J. Geophys. Res. 93, 2047–2052.

Walter, A.W., Weaver, C.S., 1980. Seismicity of the Coso Range, California. J. Geophys. Res. 85 (B5), 2441–2458.

Whitmarsh, R., 1997. Geologic Map of the Cactus Peak 7.5’ Quadrangle, Inyo County, California. University of Kansas, Lawrence, KS.

Wu, H., Lees, J.M., 1996. Attenuation structure of the Coso Geothermal area, California, from pulse width data of P-wave. Bull. Seismol. Soc. Am. 86, 1574–1590.

Wu, H., Lees, J.M., 1999. Three-dimensional P and S wave velocity structures of the Coso Geothermal Area, California, from microseismic traveltime data. J. Geophys. Res. 104, 13217–13233.